PNAS RESEARCH ARTICLE | CHEMISTRY OPEN ACCESS

10^6-fold faster C–H bond hydroxylation by a $Co^{III,IV}_2(\mu\text{-}O)_2$ complex [via a $Co^{III}_2(\mu\text{-}O)(\mu\text{-}OH)$ intermediate] versus its $Fe^{III}Fe^{IV}$ analog

Yan Li[a], Chase Abelson[b], Lawrence Que Jr.[b,1], and Dong Wang[a,1]

Edited by Edward Solomon, Stanford University, Stanford, CA; received May 11, 2023; accepted November 4, 2023

The hydroxylation of C–H bonds can be carried out by the high-valent $Co^{III,IV}_2(\mu\text{-}O)_2$ complex 2a supported by the tetradentate tris(2-pyridylmethyl)amine ligand via a $Co^{III}_2(\mu\text{-}O)(\mu\text{-}OH)$ intermediate (3a). Complex 3a can be independently generated either by H-atom transfer (HAT) in the reaction of 2a with phenols as the H-atom donor or protonation of its conjugate base, the $Co^{III}_2(\mu\text{-}O)_2$ complex 1a. Resonance Raman spectra of these three complexes reveal oxygen-isotope-sensitive vibrations at 560 to 590 cm^{-1} associated with the symmetric Co–O–Co stretching mode of the Co_2O_2 diamond core. Together with a Co•••Co distance of 2.78(2) Å previously identified for 1a and 2a by Extended X-ray Absorption Fine Structure (EXAFS) analysis, these results provide solid evidence for their "diamond core" structural assignments. The independent generation of 3a allows us to investigate HAT reactions of 2a with phenols in detail, measure the redox potential and pK_a of the system, and calculate the O–H bond strength ($D_{O–H}$) of 3a to shed light on the C–H bond activation reactivity of 2a. Complex 3a is found to be able to transfer its hydroxyl ligand onto the trityl radical to form the hydroxylated product, representing a direct experimental observation of such a reaction by a dinuclear cobalt complex. Surprisingly, reactivity comparisons reveal 2a to be 10^6-fold more reactive in oxidizing hydrocarbon C–H bonds than corresponding $Fe^{III,IV}_2(\mu\text{-}O)_2$ and $Mn^{III,IV}_2(\mu\text{-}O)_2$ analogs, an unexpected outcome that raises the prospects for using $Co^{III,IV}_2(\mu\text{-}O)_2$ species to oxidize alkane C–H bonds.

C–H bond hydroxylation | $Co_2(\mu\text{-}O)_2$ diamond core | high-valent dicobalt oxidant | radical rebound/coupling

Significance

Bioinspired transition metal complexes play critical roles in elucidating the role high-valent intermediates play in the mechanisms of substrate oxidations catalyzed by metalloenzymes. Herein, we characterize a $Co^{III}_2(\mu\text{-}O)(\mu\text{-}OH)$ intermediate **3a** involved in C–H bond hydroxylation by $Co^{III,IV}_2(\mu\text{-}O)_2$ species **2a**. Independent generation of **3a** enables detailed investigation of H-atom transfer reactions of **2a**, measurement of thermodynamic parameters for the system, and demonstration of the otherwise elusive oxygen recombination step of **3a** with trityl radical. Remarkably, **2a** reacts with C–H bonds at rates that are a millionfold faster than previously described corresponding $Fe^{III,IV}_2(\mu\text{-}O)_2$ and $Mn^{III,IV}_2(\mu\text{-}O)_2$ analogs.

Nonheme dinuclear iron enzymes activate O_2 to generate a variety of dioxygen-derived intermediates that subsequently carry out a broad range of substrate transformations. Representative examples of high-valent diiron intermediates where at least one iron center is in the oxidation state of +4 include soluble methane monooxygenase (**sMMO**) and Class **1a** ribonucleotide reductase (**RNR**). **sMMO** hydroxylates the very strong C–H bond of methane (105 kcal/mol) via a high-valent diiron(IV) intermediate called **Q** (1, 2). This intermediate has been described as having an $Fe^{IV}_2(\mu\text{-}O)_2$ diamond core (with an Fe•••Fe distance of 2.46 Å) (3–5) or more recently proposed instead to possess an open core structure (6, 7). On the other hand, the key intermediate **X** of Class **1a** RNR is a diiron(I-II,IV) species with a short Fe•••Fe distance at 2.78 Å (8) that has been attributed to a $Fe_2(\mu\text{-}O)(\mu\text{-}OH)$ or a $Fe_2(\mu\text{-}O)(\mu\text{-}1,1\text{-carboxylate})$ core (9).

The possible disagreements on the structural assignments of **sMMO-Q** and **RNR-X** have inspired tremendous synthetic efforts in the past decades to develop suitable biomimetic and bio-inspired high-valent $M_2(\mu\text{-}O)_2$ complexes for hydroxylating strong C–H bonds (1, 10–12). The hydroxylation of a substrate C–H bond mediated by high-valent metal-oxo complexes is a 2-e^- process that typically involves two fundamental steps: 1) the initial homolytic cleavage of a C–H bond to generate a 1-e^--reduced M–OH species and a carbon radical, denoted as the "C–H bond activation" step, followed by 2) rapid recombination of the hydroxyl group and the nascent carbon radical to form the hydroxylated C–OH product, often referred to as the "radical rebound" step (13). While C–H bond activation has been extensively investigated, direct experimental evidence for this latter step has not become available until just recently. Several groups have demonstrated that a variety of terminally bound functional groups including hydroxyl (14, 15), alkoxyl (16), amide (17, 18), and halide (19) in mononuclear metal complexes are able to react with a carbon radical to produce the functionalized product(s). However, the related chemistry for a bridging hydroxyl ligand in a proposed dinuclear system has yet to be demonstrated, despite the fact that hydroxo-bridged dinuclear complexes have been available for a variety of first-row transition metals (20–30). Intuitively, the recombination of a carbon radical with a bridging hydroxyl group would likely require the cleavage of two M–O(H) bonds, making it a more challenging process compared to that for one terminal M–OH bond.

Author affiliations: [a]Department of Chemistry and Biochemistry, Center for Biomolecular Structure and Dynamics, University of Montana, Missoula, MT 59812; and [b]Department of Chemistry and Center for Metals in Biocatalysis, University of Minnesota, Minneapolis, MN 55455

Author contributions: L.Q. and D.W. designed research; Y.L. and C.A. performed research; Y.L., C.A., L.Q., and D.W. analyzed data; and Y.L., C.A., L.Q. and D.W. wrote the paper.

The authors declare no competing interest.

This article is a PNAS Direct Submission.

[1]To whom correspondence may be addressed. Email: larryque@umn.edu or dong1.wang@umontana.edu.

This article contains supporting information online at https://www.pnas.org/lookup/suppl/doi:10.1073/pnas.2307950120/-/DCSupplemental.

Published December 12, 2023.

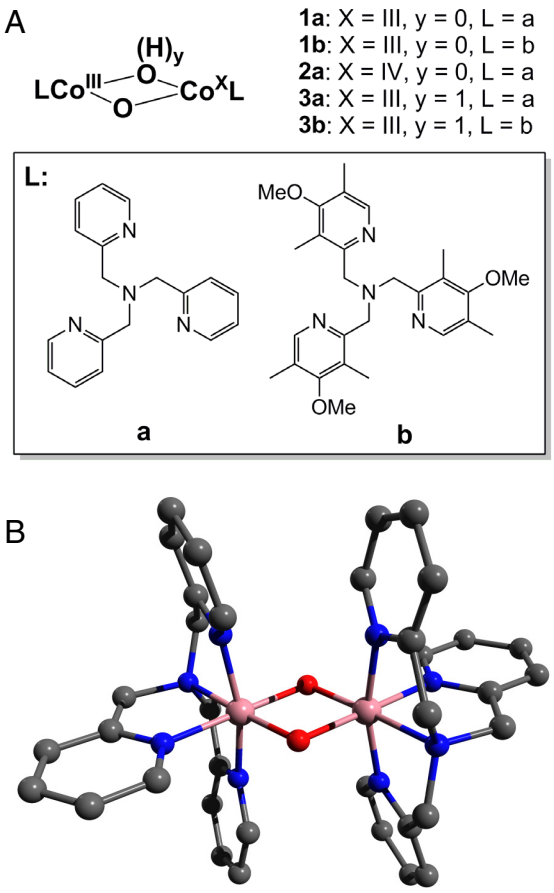

Scheme 1. (*A*) Dicobalt diamond core complexes studied in this work. (*B*) Density-functional theory (DFT)-calculated structure of **1a** first reported in ref. 31.

We have recently reported the generation and characterization of bis-μ-oxo bridged $Co^{III}_2(\mu\text{-}O)_2$ and $Co^{III,IV}_2(\mu\text{-}O)_2$ complexes (**1a** and **2a**, respectively, Scheme 1) supported by a tetradentate tris(2-pyridylmethyl)amine (TPA) ligand and demonstrated the high-valent **2a** to be capable of hydroxylating strong sp^3 C–H bonds (31). The mechanism proposed for this transformation involves 1) rate-determining C–H bond cleavage, supported by observed H/D substrate kinetic isotope effects (KIEs), to generate a putative $Co^{III}_2(O)(OH)$ species (**3a**) and a substrate radical, and 2) subsequent transfer of the hydroxyl group of **3a** to the nascent carbon radical to form the hydroxylated product. The latter step is indirectly supported by ^{18}O-labeling experiments using $H_2{}^{18}O$ that demonstrates up to ~50% ^{18}O incorporation into the hydroxylated product derived from the unlabeled $Co^{III}_2(\mu\text{-}O)_2$ starting complex, indicating that **3a** is the source of the hydroxyl group (31).

In this work, we describe the generation of the monoprotonated $Co^{III}_2(\mu\text{-}O)(\mu\text{-}OH)$ species (**3a**, Scheme 1) from multiple synthetic pathways, including 1) protonation of the conjugate base **1a** and 2) reduction of **2a** by phenols. Characterization of these three dicobalt complexes using resonance Raman (rRaman) spectroscopy shows the corresponding O-isotope-sensitive vibration to fall in the range of 560 to 590 cm^{-1}, which can be assigned to the symmetric Co–O–Co stretching mode. Furthermore, the independent generation of **3a** allows us to study in detail the HAT (H-atom transfer) reactions carried out by **2a**, measure thermodynamic driving forces (redox potential and pK_a), and investigate the reaction between **3a** and the trityl radical. Our data have provided convincing evidence showing that complex **3a** is the dicobalt(III) intermediate involved in the course of C–H bond hydroxylation mediated by its high-valent derivative **2a**. Furthermore, we have provided solid evidence showing that **3a** can transfer its bridging hydroxyl group onto a carbon radical, representing a direct experimental observation for this classical reaction carried out by a dinuclear complex, which has yet to be independently demonstrated for previously reported dinuclear Mn and Fe systems. Remarkably **2a** is shown to be a millionfold more reactive in oxidizing hydrocarbon C–H bonds than corresponding $Fe^{III,IV}_2(\mu\text{-}O)_2$ and $Mn^{III,IV}_2(\mu\text{-}O)_2$ analogs.

Results and Discussion

Characterization of $Co^{III}_2(\mu\text{-}O)_2$ and $Co^{III,IV}_2(\mu\text{-}O)_2$ Complexes by rRaman Spectroscopy. The starting complex $Co^{III}_2(\mu\text{-}O)_2$ (**1a**) and its one-electron oxidized derivative $Co^{III,IV}_2(\mu\text{-}O)_2$ (**2a**) have been characterized as complexes with bis(μ-oxo)dicobalt diamond cores by a combination of spectroscopic [^1H NMR, electrospray ionization-mass spectrometry (ESI-MS), electron paramagnetic resonance (EPR) and X-ray absorption spectroscopy (XAS)] and computational methods in our previous work (31). Key evidence for the diamond core assignment is the identification of a short Co•••Co distance at 2.78(2) Å by EXAFS analysis of **1a** and **2a** that is typically found for complexes with $M_2(\mu\text{-}O_2)$ diamond cores (32). In this work, we further characterize **1a** and **2a** using rRaman spectroscopy, which has proven to be a powerful tool to study $M_2(\mu\text{-}O)_2$ diamond core complexes (32–34). As shown in Fig. 1*A*, the rRaman spectrum of **1a** exhibits a prominent signal at 562 cm^{-1} upon excitation of its intense 460-nm absorption band, which undergoes a downshift of 21 cm^{-1} when **1a** is generated using $H_2{}^{18}O_2$. On the other hand, the higher-valent $Co^{III,IV}_2(\mu\text{-}O)_2$ complex **2a** shows an O-isotope-sensitive rRaman band at 585 cm^{-1} that downshifts to 559 cm^{-1} upon ^{18}O labeling, its 23 cm^{-1} higher energy vibration relative to that of **1a** being congruent with its increased oxidation state. These values compare favorably with the correlation between the ν_{sym}(M–O–M) and the M–O–M angle (Fig. 1*B* and Table 1). These observations are fully consistent with their assignments to symmetric M–O–M stretching modes and corroborate the symmetric nature of the diamond cores for both **1a** and **2a**, with two equivalent cobalt centers. As a consequence, the mixed-valent complex **2a** would be best described as a valence-delocalized species, consistent with spectroscopic and computational results obtained in our previous work (31). Therefore, our rRaman results, together with a Co•••Co distance of 2.78(2) Å identified for **1a** and **2a** by EXAFS analysis in our previous work (31), provide solid evidence to support the assignments of **1a** and **2a** as complexes with $Co_2(\mu\text{-}O)_2$ "diamond cores".

Generation and Characterization of a $Co^{III}_2(\mu\text{-}O)(\mu\text{-}OH)$ Complex. The addition of strong acid such as triflic acid (CF_3SO_3H) and perchloric acid ($HClO_4$, CAUTION: the perchlorate salt is potentially explosive and should be handled with care!) into the methanol solution of **1a** at −60 °C leads to the formation of a species **3a** within seconds with an intense absorption maximum at 482 nm (ε = ~12,000 M^{-1} cm^{-1}, Fig. 2*A* and *SI Appendix*, Fig. S1). Complex **3a**, with a $t_{1/2}$ = ~10 min at −40 °C, is significantly less stable than **1a** ($t_{1/2}$ = ~4 h at −40 °C) but is much more stable than the high-valent derivative **2a** ($t_{1/2}$ = ~90 s at −60 °C). Complex **3a** can be converted back to **1a** with the addition of a strong base such as tetrabutylammonium hydroxide. The entire process can be repeated multiple times upon switching between the acid and base used, indicating that the conversion between **1a** and **3a** is reversible (Fig. 2*A*). Besides **3a**, no other new species is observed to form even when a large excess of acid is used to react with **1a**. A rough estimate for the acidity of **3a** using acids of different

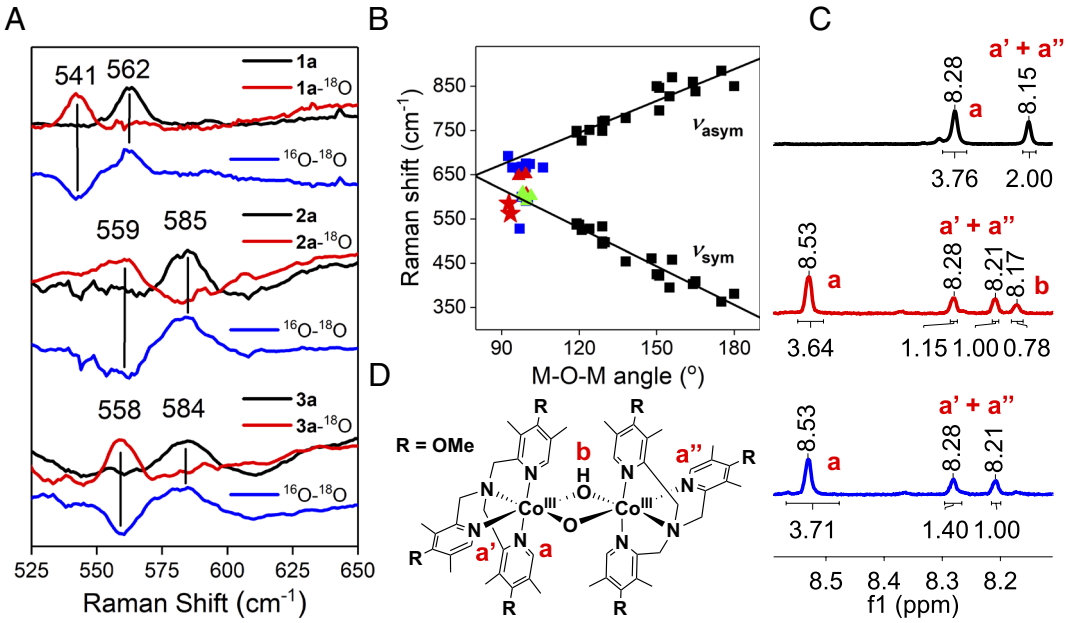

Fig. 1. (*A*) rRaman spectra of **1a** (*Top*), **2a** (*Middle*), and **3a** (*Bottom*) obtained at 193 K with 457-nm excitation. Spectra derived from $H_2{}^{16}O_2$ and $H_2{}^{18}O_2$ are shown in black and red, respectively, in each panel. The blue spectra represent the corresponding ^{16}O-^{18}O difference spectra. (*B*) Correlation between ν_{asym}(M–O–M) (*Top*) and ν_{sym}(M–O–M) (*Bottom*) values of oxo-bridged dinuclear metal complexes vs their M–O–M angles. Data from the original work of Sanders-Loehr (black squares) (33) are used to construct the linear correlations. Also included are data for complexes with $Fe_2(\mu\text{-}O)_2$ and $Fe_2(\mu\text{-}O)(\mu\text{-}OH)$ (blue squares) (22, 33, 35), $Cu_2(\mu\text{-}O)_2$ (green triangles) (36–39), and $Co_2(\mu\text{-}O)_2$ (red triangles) cores (40–42). For emphasis, the data of **1a** and **2a** obtained in this work are shown as red stars. See Table 1 and *SI Appendix*, Table S1 for more information. (*C*) The aromatic regions of the ^1H NMR spectra for **1b** (black), **3b** (red), **3b** + 10 mM D_2O (blue) obtained at −40 °C in CD_3OD. Corresponding full spectra are shown in *SI Appendix*, Fig. S11. (*D*) The proposed structure of **3b**.

strengths shows that the dissociation constant (pK_a) of **3a** is close to that of 2,2-dichloroacetic acid ($CHCl_2COOH$, pK_a = 6.38 in methanol) (47). Titration of triflic acid into the solution of **1a** further shows that only 1 eq. acid is sufficient to fully generate **3a**, indicating that **3a** is a monoprotonated derivative of **1a**. The pK_a of **3a** is more precisely determined to be 5.45 ± 0.09 by fitting the titration curve (*SI Appendix*, Fig. S2, see *SI Appendix* for more details about the titration experiment and data analysis).

Alternatively, **3a** can be obtained by the reaction of **2a** with phenol (PhOH), a hydrogen atom donor. As shown in Fig. 2*B*, the introduction of 0.075 M phenol into the methanol solution of **2a** at −60 °C affords **3a** within 20 s. The kinetic trace can be well fitted using a first-order model to obtain k_{obs} = 0.12 s^{-1}. Furthermore, the second-order rate constant k_2 of 1.18(7) M^{-1} s^{-1} for phenol oxidation can be extracted from the slope of a linear correlation between k_{obs} and the phenol concentration (*SI Appendix*, Fig. S3 and Table S2). The use of phenol-d_6 as the substrate affords k_2 = 0.36 M^{-1} s^{-1}, corresponding to a KIE of 3.3. The resulting phenoxyl radical likely dimerizes to form the dimerized phenol oxidation product. Indeed, quantification of the oxidation product(s) of 2,4-di-*tert*-butylphenol by gas chromatography–mass spectrometry (GC-MS) indicates the formation of 3,3′,5,5′-tetra-*tert*-butyl-2,2′-dihydroxybiphenyl (41% yield), accounting for ~80% of the oxidizing equivalents used. Therefore, the conversion of **2a** to **3a** is a 1-e^- + 1-H^+ process. Furthermore, the oxidation of **3a** by a one-electron oxidant such as cerium(IV) ammonium nitrate regenerates **2a**, indicating that the

Table 1. rRaman and structural data for selected diiron and dicobalt complexes

Complex*	Spin state	ν_{sym} (cm^{-1})†	ν_{asym}(cm^{-1})†	<M–O–M (°)‡	M•••M (Å)‡	Ref.
$[Fe^{III}{}_2(\mu\text{-}O)_2(6\text{-}Me_3TPA)_2]^{2+}$	0 [5/2, 5/2]		692 (−32)	92.5	2.71	(33, 43)
$[Fe^{III}Fe^{IV}(\mu\text{-}O)_2(5\text{-}Et_3TPA)_2]^{3+}$	3/2 [1/2, 1]		666 (−35)	94.1	2.68	(44, 45)
$[Fe^{IV}{}_2(\mu\text{-}O)_2(TPA^*)_2]^{4+}$	0 [1, 1]		674 (−30)	101¶	2.73§	(35)
$Fe^{III}{}_2(\mu\text{-}O)(\mu\text{-}OH)(6\text{-}Me_3\text{-}TPA)_2]^{3+}$	0 [5/2, 5/2]	591 (−27)	675 (−30) 666 (−32)	99.4	2.95	(22)
$[Co^{III}{}_2(\mu\text{-}O)_2(TPA)_2]^{2+}$ (**1a**)	0 [0, 0]	562 (−21)		93.4¶	2.78§	This work
$[Co^{III,IV}{}_2(\mu\text{-}O)_2(TPA)_2]^{3+}$ (**2a**)	1/2 [0, 1/2]	585 (−26)		92.8¶	2.78§	This work
$[Co^{III}{}_2(\mu\text{-}O)(\mu\text{-}OH)(TPA)_2]^{3+}$ (**3a**)	0 [0, 0]	584 (−26)		N.A.#	N.A.#	This work
$[Co^{III}{}_2(\mu\text{-}O)_2(L1)_2]^{2+}$	0 [1, 1]		607 (−28)	96.6	2.74	(41)
$[Co^{III}{}_2(\mu\text{-}O)_2(L2)_2]^{2+}$	N.A.#		647 (−27)	99.3	2.67	(42)
$Co^{III}{}_2(\mu\text{-}O)_2(Tp^-)_2$	N.A.#		651 (−34)	99.5	2.73	(40, 46)

Ligand abbreviations: TPA, tris(2-pyridylmethyl)amine; 6-Me_3-TPA, tris(6-methyl-2-pyridylmethyl)amine; 5-Et_3-TPA, tris(5-ethyl-2-pyridylmethyl)amine; TPA, tris(4-methoxy-3,5-dimethyl-2-pyridylmethyl)amine; Tp, hydrotris(3,5-diisopropyl-1-pyrazolyl)borate monoanion; L1, *N,N*′′-1,2-ethanediylbis[*N*′-(1,1-dimethylethyl)-urea; L2, *N,N*′-bis(2,6-diisopropylphenyl)-1,3-propanediamine.
†Numbers in the parentheses represent the shift upon ^{18}O labeling.
‡Determined by X-ray crystallography unless stated otherwise.
§Determined by EXAFS analysis.
¶Calculated using M-O and M-M distances from EXAFS results.
#N.A. = not available.

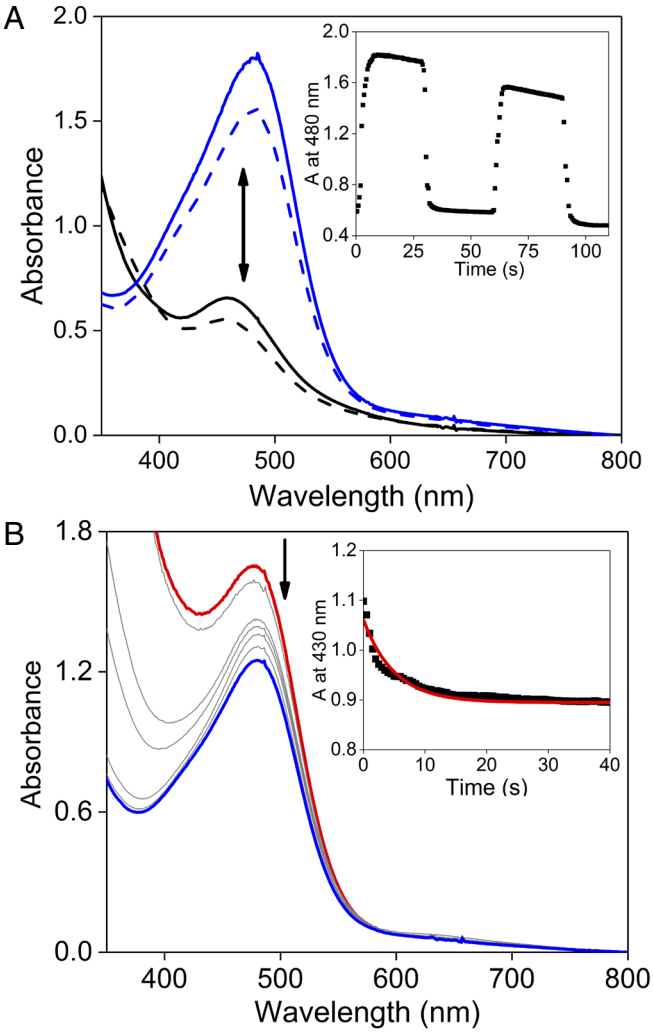

Fig. 2. (*A*) Changes in the optical spectra observed in the interconversion between 0.15 mM **1a** (blue) and **3a** (black) at −60 °C. Intensities of the dashed spectra are reduced due to dilution and slight decomposition. (*Inset*) time trace for the decay of 480-nm band. (*B*) Spectral changes observed in the reaction of 0.15 mM **2a** (red) with 0.075 M phenol at −60 °C. (*Inset*) time trace for the decay of the absorption at 430 nm, best fitted to a first-order exponential decay (red curve).

conversion between **2a** and **3a** is also reversible (*SI Appendix*, Fig. S4). Taken together, our observations demonstrate that **3a** differs from **1a** and **2a** by only one proton and one H-atom, respectively.

The overall phenol oxidation by **2a** to generate **3a** is strongly affected by the electronic properties of the phenol substrates (*SI Appendix*, Table S2). With the use of phenol derivatives (^{X}PhOH; X = OMe, Me, H, Cl and CF_3) with a variety of *para*-substituents as a set of test substrates, we have found the substrates with electron-donating groups to react faster with **2a** compared to those with electron-withdrawing groups (*SI Appendix*, Figs. S5–S8), as expected. The Hammett plot (Fig. 3*A*) clearly shows that the values of log k_2 for these reactions correlate linearly as a function of the Hammett parameter σ_{para} for the aromatic substituents with a slope of $\rho = -1.82$ ($R^2 = 0.99$). The negative ρ value is consistent with the electrophilic nature of the high-valent oxidant **2a** (*SI Appendix*, Table S3). Further analysis of the phenol oxidation results using a Marcus plot of (RT/F)ln(k_2) vs. the oxidation potential (E_{ox}) of the phenols (Fig. 3*B*) shows a reasonable linear correlation with a slope of −0.09. The slope of this plot has been discussed and related to the general mechanisms of such 1-e^- + 1-H^+ processes (48–50). The near-zero slope observed in our system is indicative of an HAT mechanism for phenol oxidation by **2a**. Furthermore, a classical BDE plot of log k_2 as a function of the phenol O–H bond strength affords a linear correlation with a slope of −0.15 (Fig. 3*C*). Interestingly, this value is almost identical to −0.17, the value observed for a related BDE plot of C–H bond oxidation by **2a** described in our earlier work (31), indicating that **2a** reacts with these two types of substrates (having O–H and C–H bonds) via related HAT mechanisms.

We have then sought to characterize **3a** in order to better understand its structural properties. Unfortunately, its short lifetime even at cryogenic temperatures hampers the growth of single crystals for X-ray crystallography. Instead, characterization of **3a** using rRaman spectroscopy (Fig. 1*A*) shows an isotope-sensitive band at 584 cm^{-1} that undergoes a downshift of −26 cm^{-1} upon ^{18}O labeling. This 584-cm^{-1} value is essentially identical to that observed for **2a**, indicating comparable M–O–M angles. Not surprisingly, these Co–O–Co values are also comparable to those of the symmetric stretching modes associated with a number of previously reported Fe^{III}_2(μ-O)(μ-OH) complexes (Table 1) and thus fully consistent with its assignment as the symmetric Co–O–Co vibration (22), clearly indicating that complex **3a** retains the diamond core structures found for **1a** and **2a**.

^{1}H NMR spectroscopy provides further structural insight into **3a**. To simplify data analysis and interpretation, we have replaced the parent TPA ligand with TPA* (ligand b, Scheme 1 *A*) with the installation of 3,5-dimethyl-4-methoxyl substituents onto the pyridine rings. These modifications remove the complexity of spin-spin coupling among the multiple aromatic protons present in **1a**, leaving only one type of aromatic proton on each of the pyridine rings. We first synthesized the mononuclear Co(II) starting complex [(TPA*)Co^{II}-Cl]$^+$ and obtained its crystal structure (*SI Appendix*, Fig. S9), which exhibits a trigonal bipyramidal

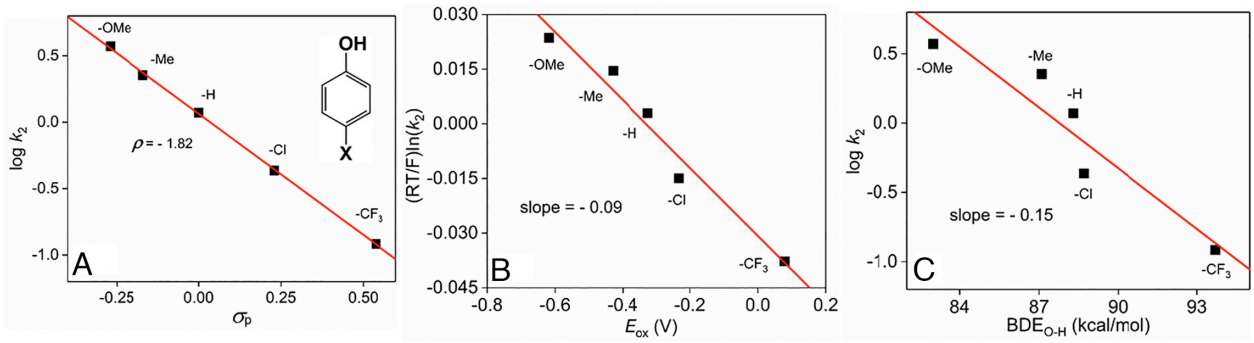

Fig. 3. (*A*) Hammett correlation, (*B*) Marcus plot of (RT/F)lnk_2 vs. E_{ox}(^{X}PhO$^{\bullet}$/^{X}PhOH), and (*C*) BDE plot of logk_2 vs. the phenol O–H bond strength for the reaction of **2a** with *para*-X-substituted phenol derivatives.

geometry similar to that found for the $[(TPA)Co^{II}\text{-}Cl]^+$ analog. By following a similar protocol for generating **1a**, we observe the stoichiometric reaction of $2[(TPA^*)Co^{II}\text{-}Cl]^+ + H_2O_2 + 2OH^-$ to form **1b** (*SI Appendix*, Fig. S10). As shown in Fig. 1*C* (aromatic region) and *SI Appendix*, Fig. S11 (full spectrum), the ^{1}H NMR spectrum of **1b** collected at −40 °C in CD_3OD exhibits two distinct singlets in the aromatic region at 8.28 and 8.15 ppm with an integration ratio of 2:1, suggesting that the three pyridines of each TPA* ligand are in two different environments – two (axial) are *trans* to each other and the third one (equatorial) is *trans* to a bridging oxo ligand. This pattern is similar to that of **1a** reported in our previous publication (31). Interestingly, adding triflic acid to convert **1b** to **3b** (*SI Appendix*, Fig. S12) gives rise to four aromatic resonances with an integration ratio of 4:1:1:1 (Fig. 1*C*, red). The signal at 8.17 ppm disappears completely upon addition of 10 mM D_2O into the solution (Fig. 1*C*, blue), indicating that this signal is assignable to the proton on the hydroxyl bridge that is exchangeable with the added D_2O. Its chemical shift is in good agreement with that of the μ-OH proton (6.7 to 7.8 ppm) reported recently for a series of coordinatively saturated $Co^{III}{}_2(\mu\text{-}OH)_2$ complexes (23). Furthermore, the splitting of the signal at 8.15 ppm observed for **1b** into two smaller peaks (8.28 and 8.21 ppm) identified for **3b** shows that the two equatorial pyridines in **1b** have become inequivalent in **3b** upon protonation of one of the two oxo bridges in **1b** (Fig. 1*C*, red). As shown in our previous DFT calculations (31), the $Co^{III}{}_2(\mu\text{-}O)_2$ diamond core complex can adopt two structural isomers differing in the relative positions of two equatorial pyridines (*trans* vs. *cis*), where the *trans*-isomer is slightly more stable than the *cis*-isomer. It is thus expected that protonation of one bridging oxo ligand would break the equivalency of the equatorial pyridines, but only for the *trans*-isomer and not for the *cis*-isomer. Therefore, our ^{1}H NMR results provide strong evidence for the structural assignment of **3b** as a monoprotonated $(TPA^*)Co^{III}(\mu\text{-}O)(\mu\text{-}OH)Co^{III}(TPA^*)$ species with a *trans*-configuration for the equatorial pyridines (Fig. 1*D*). Moreover, **3a** and **3b** should have the same diamond core structure, given the similarities in their optical spectra and essentially the same TPA ligand frameworks.

Furthermore, we have characterized **3b** using ESI-MS (*SI Appendix*, Fig. S13), showing two signals at *m/z* = 568.2166 and 1182.4220. In the ESI experiments, the formate anion ($HCOO^-$) is intentionally added in the mobile phase to pair with multi-valent cations. The stronger signal at *m/z* = 568.2166 is assigned to $[Co^{II}(TPA^*)(HCOO)]^+$ corresponding to the decomposed product of **3b**. On the other hand, the weaker signal at *m/z* = 1182.4220 shows the mass and isotope pattern assignable to $[(Co^{III}{}_2(TPA^*)_2(O)_2)^{2+}$ (**1b**) $+ H_2O + HCOO^- + CH_3CN)^+$ or $[(Co^{III}{}_2(TPA^*)_2(O)(OH))^{3+}$ (**3b**) $+ OH^- + HCOO^- + CH_3CN]^+$. These two assignments have an identical overall chemical formula but differ only in the location of one proton. Therefore, the ESI-MS data demonstrate the dinuclear nature of the cobalt complexes but cannot distinguish between **1b** and **3b**.

We have further carried out titration experiments of H_2O into the methanol solution of **3a** in order to assess the possibility of an aquation equilibrium, as observed in the diiron system (22). As shown in *SI Appendix*, Fig. S14, no new absorption feature is observed to develop upon the addition of up to 1,000 eq. H_2O. This result is in sharp contrast to the diiron analog $Fe^{III}{}_2(\mu\text{-}O)(\mu\text{-}OH)$, which undergoes core isomerization to generate an $Fe^{III}{}_2(\mu\text{-}O)(\mu\text{-}H_3O_2)$ core (22). Taken together, characterization of **3a** using rRaman and ^{1}H NMR spectroscopies as well as chemical transformations between **3a** and the other two previously described dicobalt complexes **1a** and **2a** provide strong evidence to assign **3a** as a $Co^{III}{}_2(\mu\text{-}O)(\mu\text{-}OH)$ diamond core complex and indicate only minor structural perturbations among these three dicobalt species.

Reaction of the $Co^{III}{}_2(\mu\text{-}O)(\mu\text{-}OH)$ Complex with Trityl Radical. It is notable that complex **3a** is the final product for phenol oxidation but not for the oxidation of hydrocarbons by $Co^{III,IV}{}_2(\mu\text{-}O)_2$ (**2a**). We thus hypothesize that, in the course of C–H bond hydroxylation reactions by **2a**, **3a** must be generated upon HAT from the hydrocarbon substrate to **2a** before reacting subsequently with the nascent carbon radical in the rebound step to form the hydroxylated product. In contrast, in the phenol oxidation reactions, **3a** does not react with the nascent phenoxyl radical and is thus not further consumed. Since **3a** can be generated from **1a** independently without involving **2a** and other chemical oxidants, we have sought to investigate the direct reaction between **3a** and a carbon radical. To date, a number of groups have reported that hydroxyl, alkoxyl, amide, and halide ligands in the terminal position of a mononuclear metal complex are able to react with the trityl radical ($Ph_3C\bullet$) to produce the corresponding functionalized product(s) (14–19). However, the related chemistry for a bridging hydroxyl ligand in a dinuclear system has yet to be demonstrated. Trityl radical [in equilibrium with its dimeric form: $2\ Ph_3C\bullet \rightleftharpoons (Ph_3C)_2$ (~2% $Ph_3C\bullet$ at 23 °C)] is relatively stable in organic solutions and is thus best suited for this study. As shown in Fig. 4*A*, the introduction of 6.85 mM $(Ph_3C)_2$ (the highest concentration obtainable in MeOH at −40 °C, which makes it difficult to obtain data for a set of concentration dependence experiments) into the methanol solution of **3a** at −40 °C increases the first-order decay rate (k_{obs}) of **3a** from 0.0027 to 0.0035 s^{-1}. Analysis of the reaction product using ^{1}H NMR spectroscopy (*SI Appendix*, Fig. S15) and GC-MS (*SI Appendix*, Fig. S16) shows that trityl alcohol (Ph_3COH) is formed in a reasonable yield (26% and 23% based on results obtained from ^{1}H NMR and GC-MS, respectively) (51), consistent with the kinetic measurements showing that ~25% of the overall rate is due to the reaction of **3a** with $(Ph_3C)_2$. Ph_3COH is also formed in comparable yield when the reaction is carried out under anaerobic conditions. By contrast, control experiments (*SI Appendix*, Fig. S16) show that in an aerobic solution only a trace amount of trityl alcohol is produced in the background reaction(s) of the trityl radical. Therefore, the formation of Ph_3COH is clearly the result of the trityl radical reacting with **3a** but not with O_2.

We have prepared ^{18}O-labeled **3a** from ^{18}O-enriched **1a** employing the isotope labeling protocol we reported previously using $H_2{}^{18}O$ (not $H_2{}^{18}O_2$) as the ^{18}O source (see *SI Appendix* for more details about ^{18}O-labeling procedures) (31) and then protonating **1a** to convert it to **3a**. However, the inertness of low-spin Co(III) makes the ^{18}O exchange process quite slow, even in the presence of a large excess amount of $H_2{}^{18}O$, so only a maximal 50 to 60% incorporation of ^{18}O into the diamond core can be attained before significant decay of **1a** is observed. Accordingly, we have found ^{18}O-enriched **3a** to react with $Ph_3C\bullet$ to afford $Ph_3C^{18}OH$ with only 55% incorporation of ^{18}O-isotope (*SI Appendix*, Fig. S17). These data provide strong support for the nature of **3a** as we have formulated it and argue against alternative assignments of **3a** as a (mononuclear or dinuclear) peroxo- or superoxo- complex as the oxygen exchange of $H_2{}^{18}O$ with these $Co\text{-}O_2$ adducts is highly unlikely (55). A conceivable alternative pathway to form $Ph_3C^{18}OH$ is to oxidize $Ph_3C\bullet$ by one-electron to first generate the trityl cation Ph_3C^+, followed by nucleophilic attack of $H_2{}^{18}O$ and subsequent deprotonation. However, with methanol as the solvent, Ph_3C^+ if formed should also have generated Ph_3COMe as a by-product, but the latter has not been identified as a reaction product, clearly excluding the cation pathway as responsible for the formation of

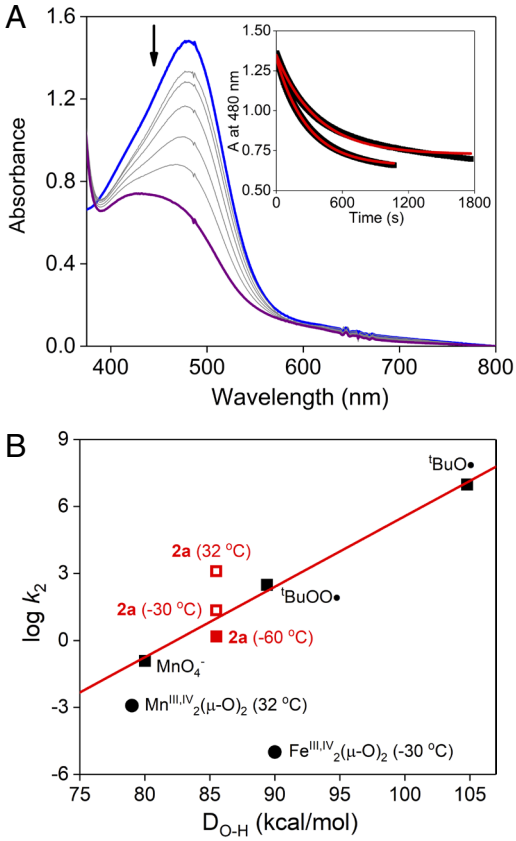

Fig. 4. (*A*) Changes observed in the optical spectra for the reaction of 0.15 mM **3a** (blue) with 6.85 mM $(Ph_3C)_2$ at −40 °C. (*Inset*) time traces at 480 nm (black) and first-order fits (red) for the decay of 3a without $(Ph_3C)_2$ (*Top*) and with added $(Ph_3C)_2$ (*Bottom*). (*B*) Plot of log k_2 for DHA oxidation vs. the strength of the O–H bond formed by the oxidants at 25 °C, unless labeled otherwise. The red straight line is defined by the entries for MnO_4^- and the two oxygen radicals (black squares) obtained from ref. 52. Additional data for $Fe^{III,IV}_2(\mu\text{-}O)_2$ and $Mn^{III,IV}_2(\mu\text{-}O)_2$ complexes (black circles) are from refs. 53 and 54, respectively. Data points for **2a** are either obtained from kinetic measurements at −60 °C (red filled square, ref. 31) or by extrapolation from the Eyring plot shown in *SI Appendix*, Fig. S19 to −30 °C and 32 °C (red open squares).

$Ph_3C^{18}OH$. Furthermore, the formation of $H^{18}O$• radical (from $H_2{}^{18}O$) that reacts with Ph_3C• to afford $Ph_3C^{18}OH$ can be excluded because no other chemical oxidant is involved in the reaction and one-electron oxidation of water to generate the hydroxyl radical is not facile. Taken together, our results provide solid evidence for hydroxyl group transfer from **3a** to the trityl radical to form the hydroxylated product.

Unfortunately, the poor solubility of the $(Ph_3C)_2$ dimer in methanol at cryogenic temperatures has prevented us from performing concentration dependence studies in order to measure the k_2 value for its reaction with **3a**. Instead, the rate enhancement of 0.0008 s^{-1} at a dimer concentration of 6.85 mM with 2% radical production yield allows us to estimate a k_2 of 5.8 M^{-1} s^{-1} for the reaction of **3a** with the trityl radical at −40 °C. This rate is about one order of magnitude higher than that for the cleavage of the C–H bond of triphenylmethane by **2a** (k_2 = 0.65(7) M^{-1} s^{-1}, *SI Appendix*, Fig. S18); the latter reaction affords Ph_3COH as the only product (53% yield). Therefore, our results provide direct experimental evidence for a rate-determining C–H bond cleavage step in the overall hydroxylation reaction. Because the reaction with Ph_3C• corresponds to a 1-e^- reduction of the dicobalt center, complex **3a** should first convert to a dicobalt(II,III) product, which likely undergoes further decomposition to generate a mixture of its mononuclear Co(II) and Co(III) components. Indeed, characterization of the cobalt products following this reaction using ^{1}H NMR spectroscopy shows the presence of both mononuclear Co(II) and Co(III) species (*SI Appendix*, Fig. S19).

Insights for C–H Bond Activation by a $Co^{III,IV}_2(\mu\text{-}O)_2$ Complex. The characterization of the monoprotonated $Co^{III}_2(\mu\text{-}O)(\mu\text{-}OH)$ species **3a** provides an opportunity to investigate thermodynamic driving forces for C–H bond activation by the high-valent $Co^{III,IV}_2(\mu\text{-}O)_2$ derivative **2a**. Specifically, **3a** is the immediate product formed after **2a** abstracts an H-atom from substrates (hydrocarbon or phenol). Therefore, determining the O–H bond dissociation energy (D_{O-H}) of **3a** is critical to assess the C–H bond cleaving reactivity of **2a**. Based on the Bordwell–Polanyi relationship shown below,

$$D_{O-H}(\mathbf{3a}) = 23.06E\,(\mathbf{2a}/\mathbf{1a}) + 1.37pK_a(\mathbf{3a}) + C, \quad [1]$$

which has been applied to numerous metal-oxo complexes (56–58), D_{O-H}(**3a**) can be calculated from the redox potential (E) of the **2a/1a** couple and the pK_a of **3a**. As we reported previously, **2a** reacts with acetylferrocene (E = 0.27 V) but not with diacetylferrocene (E = 0.49 V), so E(**2a/1a**) corresponds to a potential within the range of 0.27 to 0.49 V vs. ferrocene (31). On the other hand, pK_a(**3a**) = 5.45, as determined by acid titration (*SI Appendix*, Fig. S2). Using these values, we have calculated D_{O-H}(**3a**) to fall into the range of 83-88 kcal/mol, fully consistent with the experimental observation that **2a** can cleave C–H bonds as strong as those in ethylbenzene (87 kcal/mol) (31).

Notably, both the thermodynamic parameters and C–H bond activation reactivities are available also for a limited number of $M^{III,IV}_2(\mu\text{-}O)_2$ complexes (M = Mn and Fe) in published work (Table 2) (21, 22, 53, 54), allowing comparisons to be made among diamond core complexes of these three metal ions, although some caution should be taken in data interpretation, as the various measurements were carried out in different labs using different solvents at different temperatures. Table 2 shows that redox potentials for the Co and Fe diamond cores supported by the TPA ligand fall into the same range of 0.27 to -0.49 V vs. ferrocene, while that for the Mn diamond core supported by 1,10-phenanthroline is notably lower. On the other hand, the pK_a value determined for **3a** in methanol is ~10 units lower than those found for the Fe and Mn analogs in acetonitrile; however, as pK_a values are highly dependent on solvent, this difference is largely offset by the values of C in the calculation of D_{O-H} (**Eq. 1**). As a result, the estimated O–H bond strengths for these three $M^{III}_2(\mu\text{-}O)(\mu\text{-}OH)$ complexes likely follow the order of Fe > Co > Mn (Fig. 4*B*). In contrast, the C–H bond activation reactivities for corresponding $M^{III,IV}_2(\mu\text{-}O)_2$ complexes are distinct. As reported in our previous work (31), we have measured the rates for 9,10-dihydroanthracene (DHA) oxidation from −55 to −70 °C to construct an Eyring plot (*SI Appendix*, Fig. S20) that allows us to extrapolate the DHA oxidation rates to higher temperatures for comparison with those of other diamond core complexes. As clearly shown in Table 2, **2a** exhibits a remarkably high rate for DHA oxidation that is 6 orders of magnitude faster than those reported for $Fe^{III,IV}_2(\mu\text{-}O)_2$ and $Mn^{III,IV}_2(\mu\text{-}O)_2$ analogs at their corresponding temperatures, namely −30 °C for $Fe^{III,IV}_2(\mu\text{-}O)_2$ and +32 °C for $Mn^{III,IV}_2(\mu\text{-}O)_2$. Fig. 4*B* further shows a plot of log k_2 for DHA oxidation by a number of oxidants vs. the D_{O-H} values associated with them, where the straight line is defined by MnO_4^- and two organic radicals (59). It is obvious that the data points for **2a** fit onto the linear correlation or even fall above it, indicating that the C–H bond cleaving reactivity of **2a** is primarily driven by its thermodynamic driving force. In contrast, $Fe^{III,IV}_2(\mu\text{-}O)_2$ and $Mn^{III,IV}_2(\mu\text{-}O)_2$ complexes react at significantly slower rates, suggesting that their reactivities may be

Table 2. Comparisons of thermodynamic parameters and rate constants for DHA oxidation for diamond core complexes of Mn, Fe, and Co

Complex*	E (V)†	pK_a‡	C§	$D_{O\text{-}H}$ (kcal/mol)¶	$k_{2,DHA}$ ($M^{-1}s^{-1}$)# [T (°C)]	Solvent	Ref.
$Co^{III,IV}{}_2(\mu\text{-}O)_2$	0.27 to 0.49	5.45	69.1	83 to 88	1.5 [−60] 22 [−30]‖ 1.2×10^3 (32)‖	MeOH	(31) This work
$Fe^{III,IV}{}_2(\mu\text{-}O)_2$	0.27 to 0.49	16	59.4	87 to 93	1.0×10^{-5} [−30]	MeCN	(22), (53)
$Mn^{III,IV}{}_2(\mu\text{-}O)_2$	−0.01	14.6	59.4	79	1.2×10^{-3} [32]	MeCN	(21), (54)

*Ligand used for each complex, Co: TPA; Fe: TPA; Mn: 1,10-phenanthroline (phen).
†Redox potential of the $M^{III,IV}{}_2(\mu\text{-}O)_2/M^{III}{}_2(\mu\text{-}O)_2$ couple, ferrocene as the reference.
‡pK_a of the $M^{III}{}_2(\mu\text{-}O)(\mu\text{-}OH)$ complex.
§From ref. 58.
¶O-H bond strength of the $M^{III}{}_2(\mu\text{-}O)(\mu\text{-}OH)$ complex.
#Second-order rate constant for DHA oxidation by $M^{III,IV}{}_2(\mu\text{-}O)_2$.
‖Extrapolated from the Eyring plot shown in *SI Appendix*, Fig. S19.

hampered by additional kinetic barriers not present in the Co analog.

We propose a mechanistic scheme (Scheme 2) that summarizes all experimental observations in this work. Our results clearly demonstrate that the hydroxylation of a C–H bond by the high-valent $Co^{III,IV}{}_2(\mu\text{-}O)_2$ oxidant **2a** occurs by H-atom abstraction to form in the initial step the $Co^{III}{}_2(\mu\text{-}O)(\mu\text{-}OH)$ intermediate and a carbon radical. In particular, the demonstration that a bridging hydroxyl ligand can be transferred onto a carbon radical provides an experimental support for this classical mechanism proposed in dinuclear systems. This process may proceed by a simultaneous or stepwise cleavage of two Co–O bonds in the Co^{III}–O(H)–Co^{III} motif; neither pathway can be ruled out by our present data. The stepwise mechanism would require the bridging hydroxyl ligand to first become terminal and then react with the carbon radical. This isomerization may be triggered only when the carbon radical is present. We would argue that the presence of a rapid equilibrium between the two isomers (with a bridging vs. terminal hydroxyl ligand) would seem unlikely because 1) low spin d^6 Co(III) is well known for its inertness in ligand exchange reactions, and 2) **3a** [$Co^{III}{}_2(\mu\text{-}O)(\mu\text{-}OH)$] does not convert to a $Co^{III}{}_2(\mu\text{-}O)(\mu\text{-}O_2H_3)$ core (as observed in corresponding diiron chemistry with a terminal hydroxyl ligand that is H-bound to the adjacent bound water ligand) even in the presence of 1,000 eq. H_2O). Surprisingly, **3a** couples with $Ph_3C\bullet$ at −40 °C at a rate comparable to that of a mononuclear HO-Fe^{IV}(corrole) complex reported by Goldberg at room temperature (14) and more facile than observed for Fe^{III}–OH and Fe^{III}–OMe complexes at room temperature (15, 16, 60). These observations suggest that the coordination mode (terminal vs. bridging) of the hydroxyl ligand

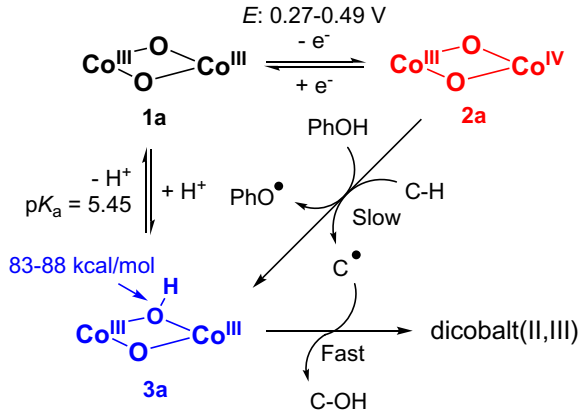

Scheme 2. Schematic illustration for the transformations of the dicobalt species **1a** to **3a** in this work.

and the oxidation state of the metal center are not the only factors that govern the reaction rates of these metal complexes with the trityl radical.

Conclusion

In summary, we have generated and characterized a $Co^{III}{}_2(\mu\text{-}O)(\mu\text{-}OH)$ species **3a** and obtained experimental evidence showing **3a** to be the intermediate involved in C–H bond hydroxylation by its high-valent $Co^{III,IV}{}_2(\mu\text{-}O)_2$ derivative **2a**. Complex **3a** can be obtained by multiple synthetic routes, including protonation of its conjugate base $Co^{III}{}_2(\mu\text{-}O)_2$ (**1a**) and reduction of **2a** by phenols. The characterization of this series of three dicobalt complexes by rRaman spectroscopy has provided confirmatory evidence for their diamond core structures, while the ^{1}H NMR spectrum of **3a** reveals a diamagnetic dicobalt(III) species with a $Co_2(\mu\text{-}O)(\mu\text{-}OH)$ core that gives rise to distinct signals from the inequivalent equatorial pyridines a' and a" (Fig. 1*C*). The independent generation of this species represents a significant development, enabling us to a) investigate in detail the HAT reactions of **2a** with phenols, b) measure the thermodynamic parameters (redox potential and pK_a) of the system in order to calculate the O–H bond strength [$D_{O\text{–}H}$(**3a**)], and c) probe the reaction between **3a** and trityl radical to generate the alcohol product. Specifically, $D_{O\text{–}H}$(**3a**) is estimated to be 83 to 88 kcal/mol, which is consistent with the observation that **2a** can cleave C–H bonds of up to 87 kcal/mol.

Notably, **3a** is able to transfer its hydroxyl ligand onto a carbon radical substrate (trityl radical) to afford the hydroxylated product in quantitative yield, which is further confirmed by ^{18}O-labeling experiments. This result represents a direct experimental observation of such a reaction involving a bridging hydroxyl ligand in a dinuclear complex. Surprisingly, the estimated reaction rate of **3a** is comparable to or even faster than those determined for mononuclear Fe complexes (14–16, 60) suggesting that the reaction with a carbon radical by a bridging group in dinuclear complexes might not be as difficult as previously assumed.

Remarkably, a comparison of DHA oxidations by related MnMn, FeFe and CoCo diamond core complexes reveals the $Co^{III,IV}{}_2(\mu\text{-}O)_2$ complex to have reaction rates 6 orders of magnitude faster than $Fe^{III,IV}{}_2(\mu\text{-}O)_2$ (at −30 °C) as well as $Mn^{III,IV}{}_2(\mu\text{-}O)_2$ (at +32 °C) analogs (Table 2). This enormous difference demonstrates that Fe and Mn diamond cores likely have larger kinetic barriers than **2a** for mediating C–H bond activation reactions. A rationale for the observed significantly higher reactivity of the CoCo complex has not been formulated and will be the target of future efforts. Taken together, our results provide valuable insights

that lead to a better understanding of how nonheme diiron enzymes hydroxylate strong sp^3 C–H bonds.

Materials and Methods

A detailed Materials and Methods section can be found in *SI Appendix*. This section includes the detailed experimental procedures for the synthesis of our complexes, kinetic measurements, acid titration and data analysis, and ^{18}O labeling experiments and product analysis. Additional figures and tables containing supporting data to the main text are also provided, including characterization of our complexes by UV-vis and ^1H NMR spectroscopies, determination of kinetic rate constants, GC-MS results for product analysis, and the crystal structure of a Co(II) starting complex (CCDC deposit number 2144749).

Data, Materials, and Software Availability. All data for this work are included in the article and *SI Appendix*.

ACKNOWLEDGMENTS. Portions of the paper were developed from the PhD thesis of Dr. Yan Li at the University of Montana (https://scholarworks.umt.edu/etd/12074). Support of this work was provided to Y.L. and D.W. by the University of Montana, Montana INBRE (IDeA Networks of Biomedical Research Excellence, grant NIGMS P20GM103474) and the NSF (grant CHE-2102339). Support of this work at the University of Minnesota was provided to L.Q. by the NIH (grant R35 GM-131721).

1. A. J. Jasniewski, L. Que Jr., Dioxygen activation by nonheme diiron enzymes: Diverse dioxygen adducts, high-valent intermediates, and related model complexes. *Chem. Rev.* **118**, 2554–2592 (2018).
2. S. Friedle, E. Reisner, S. J. Lippard, Current challenges of modeling diiron enzyme active sites for dioxygen activation by biomimetic synthetic complexes. *Chem. Soc. Rev.* **39**, 2768–2779 (2010).
3. L. Shu *et al.*, An $Fe^{IV}_2O_2$ diamond core structure for the key intermediate Q of methane monooxygenase. *Science* **275**, 515–518 (1997).
4. R. Banerjee, Y. Proshlyakov, J. D. Lipscomb, D. A. Proshlyakov, Structure of the key species in the enzymatic oxidation of methane to methanol. *Nature* **518**, 431–435 (2015).
5. A. B. Jacobs *et al.*, Nuclear resonance vibrational spectroscopic definition of the $Fe(IV)_2$ intermediate Q in methane monooxygenase and its reactivity. *J. Am. Chem. Soc.* **143**, 16007–16029 (2021).
6. G. E. Cutsail III. *et al.*, High-resolution extended X-ray absorption fine structure analysis provides evidence for a longer Fe·Fe distance in the Q intermediate of methane monooxygenase. *J. Am. Chem. Soc.* **140**, 16807–16820 (2018).
7. R. G. Castillo *et al.*, High-energy-resolution fluorescence-detected X-ray absorption of the Q intermediate of soluble methane monooxygenase. *J. Am. Chem. Soc.* **139**, 18024–18033 (2017).
8. L. M. K. Dassama *et al.*, A 2.8 Å Fe—Fe separation in the $Fe_2^{III/IV}$ intermediate, X, from Escherichia coli ribonucleotide reductase. *J. Am. Chem. Soc.* **135**, 16758–16761 (2013).
9. P. E. Doan, M. Shanmugam, J. Stubbe, B. M. Hoffman, Composition and structure of the inorganic core of relaxed intermediate X(Y122F) of Escherichia coli ribonucleotide reductase. *J. Am. Chem. Soc.* **137**, 15558–15566 (2015).
10. R. Trammell, K. Rajabimoghadam, I. Garcia-Bosch, Copper-promoted functionalization of organic molecules: From biologically relevant Cu/O_2 model systems to organometallic transformations. *Chem. Rev.* **119**, 2954–3031 (2019).
11. C. E. Elwell *et al.*, Copper—oxygen complexes revisited: Structures, spectroscopy, and reactivity. *Chem. Rev.* **117**, 2059–2107 (2017).
12. K. J. Young, B. J. Brennan, R. Tagore, G. W. Brudvig, Photosynthetic water oxidation: Insights from manganese model chemistry. *Acc. Chem. Res.* **48**, 567–574 (2015).
13. X. Huang, J. T. Groves, Beyond ferryl-mediated hydroxylation: 40 years of the rebound mechanism and C-H activation. *J. Biol. Inorg. Chem.* **22**, 185–207 (2017).
14. J. P. T. Zaragoza *et al.*, Direct observation of oxygen rebound with an iron-hydroxide complex. *J. Am. Chem. Soc.* **139**, 13640–13643 (2017).
15. V. Yadav, J. B. Gordon, M. A. Siegler, D. P. Goldberg, Dioxygen-derived nonheme mononuclear $Fe^{III}(OH)$ complex and its reactivity with carbon radicals. *J. Am. Chem. Soc.* **141**, 10148–10153 (2019).
16. T. M. Pangia *et al.*, Observation of radical rebound in a mononuclear nonheme iron model complex. *J. Am. Chem. Soc.* **140**, 4191–4194 (2018).
17. E. S. Jang *et al.*, Copper(II) anilides in sp^3 C-H amination. *J. Am. Chem. Soc.* **136**, 10930–10940 (2014).
18. D. A. Iovan, T. A. Betley, Characterization of iron-imido species relevant for N-group transfer chemistry. *J. Am. Chem. Soc.* **138**, 1983–1993 (2016).
19. J. K. Bower, A. D. Cypcar, B. Henriquez, S. C. E. Stieber, S. Zhang, $C(sp^3)$—H fluorination with a copper(II)/(III) redox couple. *J. Am. Chem. Soc.* **142**, 8514–8521 (2020).
20. M. J. Baldwin, V. L. Pecoraro, Energetics of proton-coupled electron transfer in high-valent $Mn_2(\mu\text{-}O)_2$ systems: Models for water oxidation by the oxygen-evolving complex of photosystem II. *J. Am. Chem. Soc.* **118**, 11325–11326 (1996).
21. A. S. Larsen *et al.*, Hydrocarbon oxidation by bis-μ-oxo manganese dimers: Electron transfer, hydride transfer, and hydrogen atom transfer mechanisms. *J. Am. Chem. Soc.* **124**, 10112–10123 (2002).
22. H. Zheng, Y. Zang, Y. Dong, V. G. Young Jr., L. Que Jr., Complexes with $Fe^{III}_2(\mu\text{-}O)(\mu\text{-}OH)$, $Fe^{III}_2(\mu\text{-}O)_2$, and $Fe^{III}_3(\mu\text{-}O)_3$ cores: Structures, spectroscopy, and core interconversions. *J. Am. Chem. Soc.* **121**, 2226–2235 (1999).
23. A. A. DeLucia, K. A. Kelly, K. A. Herrera, D. L. Gray, L. Olshansky, Intramolecular hydrogen-bond interactions tune reactivity in biomimetic Bis(μ-hydroxo)dicobalt complexes. *Inorg. Chem.* **60**, 15599–15609 (2021).
24. H. Kotani, D. Hong, K. Satonaka, T. Ishizuka, T. Kojima, Mechanistic insight into dioxygen evolution from diastereomeric μ-peroxo dinuclear Co(III) complexes based on stoichiometric electron-transfer oxidation. *Inorg. Chem.* **58**, 3676–3682 (2019).
25. T. Ishizuka *et al.*, Homogeneous photocatalytic water oxidation with a dinuclear Co^{III}—pyridylmethylamine complex. *Inorg. Chem.* **55**, 1154–1164 (2016).
26. H.-Y. Wang, E. Mijangos, S. Ott, A. Thapper, Water oxidation catalyzed by a dinuclear cobalt-polypyridine complex. *Angew. Chem. Int. Ed.* **53**, 14499–14502 (2014).
27. G. Spedalotto *et al.*, Preparation and characterisation of a bis-μ-hydroxo-Ni^{III}_2 complex. *Chem. Eur. J.* **25**, 11983–11990 (2019).
28. G. Spedalotto, M. Lovisari, A. R. McDonald, Reactivity properties of mixed- and high-valent bis(μ-Hydroxide)-dinickel complexes. *ACS Omega* **6**, 28162–28170 (2021).
29. G. Ali, P. E. VanNatta, D. A. Ramirez, K. M. Light, M. T. Kieber-Emmons, Thermodynamics of a μ-oxo dicopper(II) complex for hydrogen atom abstraction. *J. Am. Chem. Soc.* **139**, 18448–18451 (2017).
30. P. E. VanNatta, D. A. Ramirez, A. R. Velarde, G. Ali, M. T. Kieber-Emmons, Exceptionally high O—H bond dissociation free energy of a dicopper(II) μ-Hydroxo complex and insights into the geometric and electronic structure origins thereof. *J. Am. Chem. Soc.* **142**, 16292–16312 (2020).
31. Y. Li *et al.*, Highly reactive $Co^{III,IV}_2(\mu\text{-}O)_2$ diamond core complex that cleaves C-H bonds. *J. Am. Chem. Soc.* **141**, 20127–20136 (2019).
32. L. Que Jr., W. B. Tolman, Bis(μ-oxo)dimetal "diamond" cores in copper and iron complexes relevant to biocatalysis. *Angew. Chem. Int. Ed.* **41**, 1114–1137 (2002).
33. E. C. Wilkinson *et al.*, Raman signature of the Fe_2O_2 "diamond" core. *J. Am. Chem. Soc.* **120**, 955–962 (1998).
34. P. L. Holland *et al.*, Resonance raman spectroscopy as a probe of the bis(μ-oxo)dicopper core. *J. Am. Chem. Soc.* **122**, 792–802 (2000).
35. G. Xue *et al.*, A synthetic precedent for the $[Fe^{IV}_2(\mu\text{-}O)_2]$ diamond core proposed for methane monooxygenase intermediate **Q**. *Proc. Natl. Acad. Sci. U.S.A.* **104**, 20713–20718 (2007).
36. S. Mahapatra *et al.*, Structural, spectroscopic, and theoretical characterization of Bis(μ-oxo)dicopper complexes, novel intermediates in copper-mediated dioxygen activation. *J. Am. Chem. Soc.* **118**, 11555–11574 (1996).
37. S. Mahapatra, V. G. Young Jr., S. Kaderli, A. D. Zuberbuhler, W. B. Tolman, Tuning the structure and reactivity of the $[Cu_2(\mu\text{-}O)_2]^{2+}$ core: Characterization of a new Bis(μ-oxo)dicopper complex stabilized by a sterically hindered dinucleating Bis(triazacyclononane) ligand. *Angew. Chem. Int. Ed.* **36**, 130–133 (1997).
38. V. Mahadevan *et al.*, Irreversible reduction of dioxygen by simple peralkylated diamine-copper(I) complexes: Characterization and thermal stability of a $[Cu_2(\mu\text{-}O)_2]^{2+}$ Core. *J. Am. Chem. Soc.* **119**, 11996–11997 (1997).
39. H. Hayashi *et al.*, A Bis(μ-oxo)dicopper(III) Complex with aromatic nitrogen donors: Structural characterization and reversible conversion between copper(I) and Bis(μ-oxo)dicopper(III) species. *J. Am. Chem. Soc.* **122**, 2124–2125 (2000).
40. S. Hikichi *et al.*, Characterization of a $\mu\text{-}\eta^2\text{:}\eta^2$-peroxo dinuclear Cobalt(II) complex. *Inorg. Chem.* **36**, 266–267 (1997).
41. P. L. Larsen, T. J. Parolin, D. R. Powell, M. P. Hendrich, A. S. Borovik, Hydrogen bonds around $M(\mu\text{-}O)_2M$ rhombs: Stabilizing a $Co^{III}(\mu\text{-}O)_2Co^{III}$ complex at room temperature. *Angew. Chem. Int. Ed.* **42**, 85–89 (2003).
42. X. Engelmann *et al.*, A new domain of reactivity for high-valent dinuclear $[M(\mu\text{-}O)_2M']$ complexes in oxidation reactions. *Angew. Chem. Int. Ed.* **56**, 297–301 (2017).
43. Y. Zang, Y. Dong, L. Que Jr., K. Kauffmann, E. Münck, The first Bis(μ-oxo)diiron(III) complex. Structure and magnetic properties of $[Fe_2(\mu\text{-}O)_2(6TLA)_2](ClO_4)_2$. *J. Am. Chem. Soc.* **117**, 1169–1170 (1995).
44. H.-F. Hsu, Y. Dong, L. Shu, V. G. Young Jr., L. Que Jr., Crystal structure of a synthetic high-valent complex with an $Fe_2(\mu\text{-}O)_2$ diamond core. Implications for the core structures of methane monooxygenase intermediate Q and ribonucleotide reductase intermediate X. *J. Am. Chem. Soc.* **121**, 5230–5237 (1999).
45. A. J. Skulan, M. A. Hanson, H.-f. Hsu, L. Que Jr., E. I. Solomon, Spectroscopic study of $[Fe_2O_2(5\text{-}Et_3\text{-}TPA)_2]^{3+}$: Nature of the Fe_2O_2 Diamond core and its possible relevance to high-valent binuclear non-heme enzyme intermediates. *J. Am. Chem. Soc.* **125**, 7344–7356 (2003).
46. S. Hikichi, M. Yoshizawa, Y. Sasakura, M. Akita, Y. Moro-oka, First synthesis and structural characterization of dinuclear M(III) Bis(μ-oxo) complexes of nickel and cobalt with Hydrotris(pyrazolyl)borate ligand. *J. Am. Chem. Soc.* **120**, 10567–10568 (1998).
47. E. L. M. Miguel, P. L. Silva, J. R. Pliego, Theoretical prediction of pKa in methanol: Testing SM8 and SMD models for carboxylic acids, phenols, and amines. *J. Phys. Chem. B* **118**, 5730–5739 (2014).
48. P. Mondal, P. Pirovano, A. Das, E. R. Farquhar, A. R. McDonald, Hydrogen atom transfer by a high-valent nickel-chloride complex. *J. Am. Chem. Soc.* **140**, 1834–1841 (2018).
49. D. Unjaroen *et al.*, High-Valent d^7 Ni^{III} versus d^8 Cu^{III} Oxidants in PCET. *Inorg. Chem.* **58**, 16838–16848 (2019).
50. I. Garcia-Bosch *et al.*, Substrate and lewis acid coordination promote O—O bond cleavage of an unreactive $L_2Cu^{II}_2(O_2^{2-})$ species to form $L_2Cu^{III}_2(O)_2$ cores with enhanced oxidative reactivity. *J. Am. Chem. Soc.* **139**, 3186–3195 (2017).
51. T. Maekawa, H. Sekizawa, K. Itami, Controlled alcohol-carbonyl interconversion by nickel catalysis. *Angew. Chem. Int. Ed.* **50**, 7022–7026 (2011).
52. K. A. Gardner, L. L. Kuehnert, J. M. Mayer, Hydrogen atom abstraction by permanganate: Oxidations of arylalkanes in organic solvents. *Inorg. Chem.* **36**, 2069–2078 (1997).
53. G. Xue, R. D. Hont, E. Münck, L. Que Jr., Million-fold activation of the $[Fe_2(\mu\text{-}O)_2]$ diamond core for C-H bond cleavage. *Nat. Chem.* **2**, 400–405 (2010).
54. K. Wang, J. M. Mayer, Oxidation of hydrocarbons by $[(phen)_2Mn(\mu\text{-}O)_2Mn(phen)_2]^{3+}$ via hydrogen atom abstraction *J. Am. Chem. Soc.* **119**, 1470–1471 (1997).
55. S. Fukuzumi, K.-B. Cho, Y.-M. Lee, S. Hong, W. Nam, Mechanistic dichotomies in redox reactions of mononuclear metal–oxygen intermediates. *Chem. Soc. Rev.* **49**, 8988–9027 (2020).
56. J. M. Mayer, Understanding hydrogen atom transfer: From bond strengths to marcus theory. *Acc. Chem. Res.* **44**, 36–46 (2011).
57. J. P. Roth, J. C. Yoder, T.-J. Won, J. M. Mayer, Application of the marcus cross relation to hydrogen atom transfer reactions. *Science* **294**, 2524–2526 (2001).

58. J. J. Warren, T. A. Tronic, J. M. Mayer, Thermochemistry of proton-coupled electron transfer reagents and its implications. *Chem. Rev.* **110**, 6961–7001 (2010).
59. J. R. Bryant, J. M. Mayer, Oxidation of C-H bonds by $[(bpy)_2(py)Ru^{IV}O]^{2+}$ occurs by hydrogen atom abstraction *J. Am. Chem. Soc.* **125**, 10351–10361 (2003).
60. V. Yadav, R. J. Rodriguez, M. A. Siegler, D. P. Goldberg, Determining the inherent selectivity for carbon radical hydroxylation versus halogenation with $Fe^{III}(OH)(X)$ complexes: Relevance to the rebound step in non-heme iron halogenases. *J. Am. Chem. Soc.* **142**, 7259–7264 (2020).